Ultrasonics 104 (2020) 106108

Contents lists available at ScienceDirect

Ultrasonics

journal homepage: www.elsevier.com/locate/ultras

Deployable tessellated transducer array for ultrasound focusing and bio-heat generation in a multilayer environment

Chengzhe Zou, Ryan L. Harne*

Department of Mechanical and Aerospace Engineering, The Ohio State University, Columbus, OH 43210, USA

ARTICLE INFO

Keywords:
Wave propagation
Deployable transducer array
High intensity focused ultrasound

ABSTRACT

High intensity focused ultrasound (HIFU) has great potential to thermally ablate diseased tissues with minimal invasion. Yet, HIFU practice has limited cancer treatment potential since the absorption, diffusion, and reflection of ultrasound prevent HIFU from penetrating the body to deep and concealed diseased tissue. To explore a vision of deployable HIFU transducers, this research introduces an origami-inspired concept wherein a deployable tessellated acoustic array is employed to reduce the distance between the HIFU transducer and diseased tissues. A flat-foldable HIFU transducer array is considered, such that the compact shape is used to pass through the human body and then deployed into the operational form for treatment. Here a theoretical framework is developed to study the focusing and thermal heating capabilities of the tessellated array in a multilayer environment. It is observed that the wavefield and thermal elevation realized by the foldable array are functionally similar to those of an ideal arc-shaped transducer. Folding patterns that permit adequate curvature and high quality factor, and that balance slenderness and conformability are found to be beneficial for an ultrasound focusing practice. The efficacy of the analytical predictions are verified through direct numerical simulations. All together, the results encourage attention to foldable array concepts as potential means to advance in-vivo HIFU-based procedures.

1. Introduction

High intensity focused ultrasound (HIFU) is a promising therapeutic technique to thermally ablate diseased tissues [1]. When guided by monitoring methods such as magnetic resonance imaging [2], the focused ultrasound may converge to the target with needed precision and reduced invasion. Moreover, thermal ablation by HIFU is less risky than radiotherapy and traditional surgical removal of tumors, therefore repeated HIFU treatments are permissible [3]. Due to these advantages, HIFU is widely studied [4–6] and considered as a desirable treatment option in practice [7–11].

Despite successful applications, limitations still exist in current HIFU treatment approaches. For instance, focused acoustic energy may be reflected due to acoustic impedance mismatch along the wave propagation path, so that insufficient heat may be generated at the target location [1,3,12]. In addition, HIFU may be less effective for tissue deep in the body such that absorption along the propagation path diminishes the power of the focused ultrasound [13,14]. The aforementioned challenges originate from the distance between diseased tissues and HIFU transducers that are placed outside human body. It is envisioned that the transducer may be in the close proximity of target location by moving HIFU transducer into the body. As such, concerns regarding impedance mismatch and wave absorption are lessened, albeit not eliminated. Yet the size of existing commercial HIFU transducers prohibits such a concept from realization.

The emergence of origami science inspires a feasible solution to this problem. One intriguing attribute of origami-based design is an opportunity to govern system shape by simple folding actions. This leads to means to tailor system properties for engineered materials [15,16], antennas [17,18], and waveguides [19,20]. The shape change also permits exceptional deployability from a highly compact stowed state. Such deployability is exemplified for microgrippers [21,22], drug delivery [23], heart catheterization [24,25], and more [26]. Here, deployable tessellated acoustic arrays are expected to deliver a compacted HIFU transducer close to the point of care, where the array may be able to thermally ablate the diseased tissue by deployment. After the treatment, the compacted transducer is removed from the body by reversible folding. This report builds from recent evidence to computationally investigate the viability of a foldable array to thermally ablate tissue as a first step towards such promising practical potential.

In such acoustic arrays, the tessellated facets are considered to be normally vibrating, baffled pistons that radiate acoustic waves [27–29].

* Corresponding author.
E-mail address: harne.3@osu.edu (R.L. Harne).

https://doi.org/10.1016/j.ultras.2020.106108
Received 18 April 2019; Received in revised form 14 December 2019; Accepted 18 February 2020
Available online 24 February 2020
0041-624X/

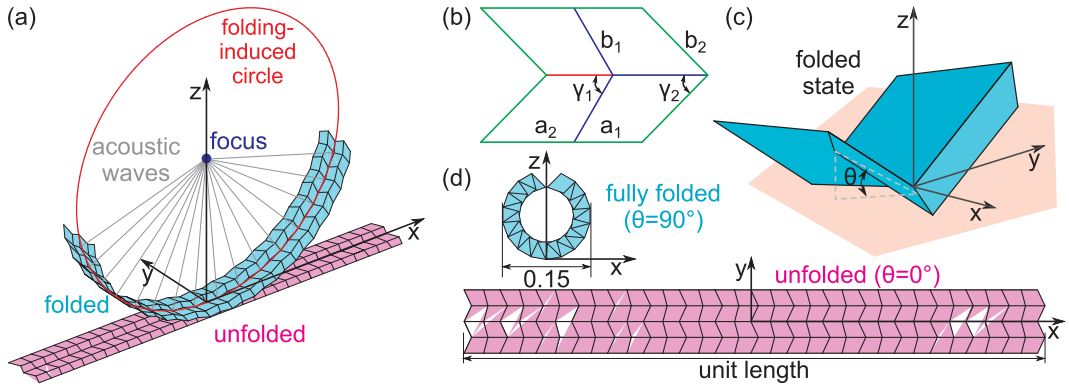

Fig. 1. Concept overview. (a) Curved array reconfigured from flat tessellation, which focuses acoustic waves near the circle center. (b) Geometric notation of unfolded unit of curved Miura-ori. (c) Folded shape of curved Miura-ori unit and folding angle θ. (d) Flat-foldability of curved Miura-ori tessellation and compactness under fully folded state.

When the tessellation is folded from the flat form in Fig. 1(a), the acoustic waves converge to the folding-induced circle center and focus acoustic energy. The tessellation employed in Fig. 1(a) is curved Miura-ori, with geometric parameters denoted in Fig. 1(b, c). The folding extent is governed by the folding angle θ, Fig. 1(c). A well-known characteristic of Miura-ori-based tessellations is flat-foldability [30], which signifies that the tessellated facets are coplanar under both states of unfolded ($x-y$ plane) and fully folded ($x-z$ plane), as shown in Fig. 1(d). In addition, for the specific tessellated array studied here, Fig. 1(d) shows that the largest dimension of the fully folded configuration is 15% of the unfolded array. This demonstrates that the folding operation would reduce the size of the working HIFU transducer by as much as 85% before deployment into the curved form shown in Fig. 1(b) for treatment. The potential of such deployability has clear advantages over existing HIFU techniques with fixed-shape spherical transducers [31,32] or phased arrays [4,5]. From the illustrations of the concept, it is apparent that reconfigurable tessellated acoustic arrays may enable new opportunities for deploying HIFU practices against diseased tissues currently unable to be treated.

This report establishes an analytical model to examine the efficacy of reconfigurable tessellated acoustic array to provide adequate heat for thermal ablation of tissue. The analytical formulation is created with acoustic and bio-heat modeling. Analytical results are investigated for evidence of thermal ablation capabilities and benchmarked against an arc-shaped HIFU transducer with more ideal focusing surfaces. A high-fidelity finite element model is then composed and the numerical simulations are compared with the analysis outcomes to verify the efficacy of the straightforward theoretical framework. Finally, a summary of research discoveries is provided along with key conclusions.

2. Analytical model formulation

Rayleigh's integral is sufficient to predict the acoustic field radiated from the acoustic transducer into an unbounded fluid medium. Yet, for HIFU treatment the ultrasound travels through a multilayered environment so that impedance differences are encountered at each interface along the path to the target. Reflection and refraction of acoustic waves may occur at such interfaces between layers. Taking into account all of these factors, here a theoretical framework is established to predict linear, continuous wave propagation from the tessellated array through a multilayer environment. The acoustic pressure determined from the analysis is then used to compute the thermal change induced in the targeted medium, according to a steady-state solution of the bio-heat transfer equation [33].

In this work, the tessellation of curved Miura-ori is employed to assemble the acoustic array. The folded geometry of the curved Miura-ori unit is defined by edge lengths a_1 and b_1, edge angles γ_1 and γ_2, and folding angle θ, Fig. 1(b, c). The dimensions a_2 and b_2 are dependent on the prior parameters [30]. For an array assembly of such units, the notations $M_x \times M_y$ are used to describe the numbers of units assembled in the x and y dimensions, respectively. For example, the tessellation shown in Fig. 1(d) has 16×2 units as active area. The folding-induced geometric reconfiguration of curved Miura-ori array is established in previous work [34], and is not repeated here for sake of brevity.

2.1. Acoustic pressure in single layer of medium

Rayleigh's integral is used to characterize the acoustic waves radiated from the oscillating surfaces of the curved Miura-ori array into the adjacent medium. The method developed by Ocheltree and Frizzell [35] is employed here to discretize each facet into sub-facets of smaller areas as shown in Fig. 2(a). To be specific, the original parallelogram facet is divided into two triangles and each triangle is discretized into four smaller triangles after once refinement. With sufficient refinement, regions of the adjacent fluid in the near field of the array are in the far field of each discretized element, which permits summation of elemental responses as point sources to determine the overall acoustic pressure. All results reported here are obtained after convergence studies that confirm the refinement of the discretized array surface leads to consistent outcome of total acoustic pressure. The rule of thumb is to guarantee at least six elements along one wavelength, while computation cost is linearly proportional with the number of triangular sub-facets.

The acoustic pressure delivered from the i^{th} baffled, vibrating sub-facet to the field point is

$$p^i = j\frac{\rho\omega u}{2\pi}\frac{e^{-jk|\mathbf{r}_i|}}{|\mathbf{r}_i|}A_i e^{\alpha\frac{\omega}{2\pi}|\mathbf{r}_i|}e^{j\omega t} \tag{1}$$

The density of the fluid is ρ; ω is the angular oscillating frequency of the facet; A_i is the area of the i^{th} sub-facet; u is the amplitude of the normal velocity over A_i; $k = \omega/c$ is the acoustic wavenumber with the sound speed c; $\mathbf{r}_i$ is the vector from the center of the i^{th} sub-facet to the field point; α is the attenuation coefficient of the medium with units (Np/m/MHz).

2.2. Acoustic pressure in multilayered media

In order to demonstrate the strategy to model the propagation of acoustic waves in multilayered media, an example of two layers is discussed here. As shown in Fig. 2(b), the reconfigurable tessellated acoustic array is located in the first layer and radiates acoustic waves into the second layer. To consider the acoustic transmission and reflection between layers, the acoustic pressure is first determined for all locations on the interface. For this purpose, the interface is discretized

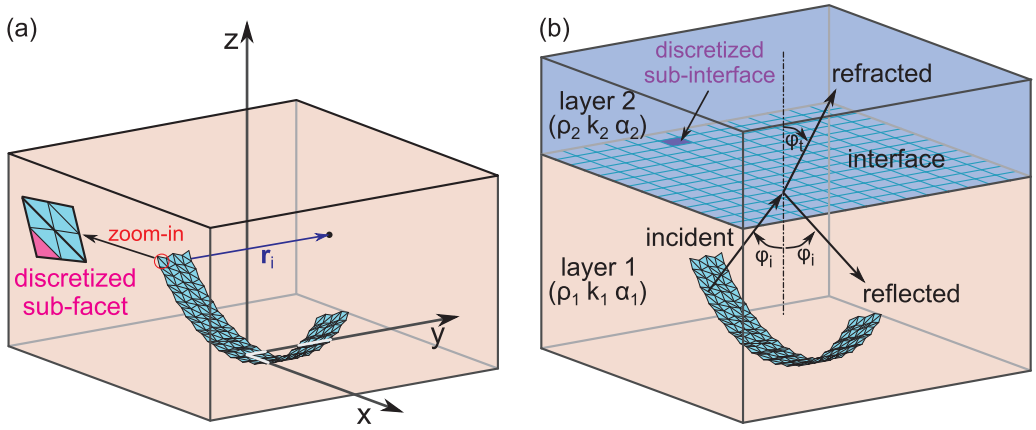

Fig. 2. Analytical notation for multilayer modeling. (a) Discretization of transducer surface into triangular sub-facets with the zoom-in of one facet as an example. (b) An environment with two layered media: discretization of interface into square sub-interfaces and definition of incidence and refraction angles.

in Fig. 2(b) to capture the distribution of acoustic pressure. Such discretization is based on the same principle as the discretization of the transducer surfaces [35,32].

The acoustic pressure on the l^{th} sub-interface due to the radiation from the i^{th} tessellated sub-facet is

$$p^{i\to l} = j\frac{\rho_1 \omega u}{2\pi}\frac{e^{-jk_1|\mathbf{r}_{il}|}}{|\mathbf{r}_{il}|}A_i e^{\alpha_1 \frac{\omega}{2\pi}|\mathbf{r}_{il}|}e^{j\omega t} \tag{2}$$

where the subscripts of ρ_1, k_1, and α_1 indicate the layer number, and $\mathbf{r}_{il}$ is the vector from the geometric center of the i^{th} sub-facet to that of the l^{th} sub-interface.

Considering the acoustic waves arriving at the interface are spherical, the magnitude of the particle velocity due to $p^{i\to l}$ in the 1st layer side of the l^{th} sub-interface is

$$u^{i\to l} = \left|\left[1 - \frac{j}{k_1|\mathbf{r}_{il}|}\right]\frac{p^{i\to l}}{\rho_1 c_1}\right| \tag{3}$$

The acoustic waves may be transmitted and reflected at the interface. The transmission and reflection coefficients of the particle velocity are respectively [12]

$$T^{i\to l} = \frac{2\rho_1 c_1 \cos\varphi_i^{i\to l}}{\rho_2 c_2 \cos\varphi_i^{i\to l} + \rho_1 c_1 \cos\varphi_t^{i\to l}} \tag{4a}$$

$$R^{i\to l} = \frac{\rho_1 c_1 \cos\varphi_t^{i\to l} - \rho_2 c_2 \cos\varphi_i^{i\to l}}{\rho_2 c_2 \cos\varphi_i^{i\to l} + \rho_1 c_1 \cos\varphi_t^{i\to l}} \tag{4b}$$

The φ_i and φ_t are the incident and refracted elevation angles, respectively, which satisfy Snell's law and are dependent on the locations of i^{th} sub-facet and l^{th} sub-interface. The problem is three-dimensional (3D) in general, although the reflection and refraction modeling for each discretized surface element is limited to the 2D plane through which each ray passes, like the example shown in Fig. 2(b). This is a special case of more general interface modeling because the interface in this study has normal vectors parallel with the z axis, Fig. 2(b). In terms of the incident vector, it is computed from the geometric center of the i^{th} sub-facet to that of the l^{th} sub-interface.

The amplitudes of the transmitted and reflected normal particle velocities on the l^{th} sub-interface due to the radiation from the i^{th} sub-facet of the tessellated acoustic array are respectively

$$u_t^{i\to l} = u^{i\to l} T^{i\to l} \cos\varphi_t^{i\to l} \tag{5a}$$

$$u_r^{i\to l} = -u^{i\to l} R^{i\to l} \cos\varphi_i^{i\to l} \tag{5b}$$

Based on linear superposition, the transmitted and reflected normal particle velocity amplitudes on the l^{th} sub-interface are respectively

$$u_t^l = \sum_{i=1}^{N} u^{i\to l} T^{i\to l} \cos\varphi_t^{i\to l} \tag{6a}$$

$$u_r^l = \sum_{i=1}^{N} -u^{i\to l} R^{i\to l} \cos\varphi_i^{i\to l} \tag{6b}$$

where N is the number of discretized sub-facets on the tessellated acoustic source.

Then the transmitted and reflected acoustic pressures from the interface are determined by superposition of all discretized interface contributions.

$$p_t = \sum_{l=1}^{L} j\frac{\rho_2 \omega u_t^l}{2\pi}\frac{e^{-jk_2|\mathbf{r}_l|}}{|\mathbf{r}_l|}A_l e^{\alpha_2 \frac{\omega}{2\pi}|\mathbf{r}_l|}e^{j\omega t} \tag{7a}$$

$$p_r = \sum_{l=1}^{L} j\frac{\rho_1 \omega \mathbf{u}_r^l}{2\pi}\frac{e^{-jk_1|\mathbf{r}_l|}}{|\mathbf{r}_l|}A_l e^{\alpha_1 \frac{\omega}{2\pi}|\mathbf{r}_l|}e^{j\omega t} \tag{7b}$$

The L is the total number of discretized sub-interfaces in the interface, and $|\mathbf{r}_l|$ is the distance between the l^{th} sub-interface and the field point that receives either transmission or reflection.

Although only two layers are discussed here, the strategy may be extended to consider a greater number of layers. As a result, the acoustic field in each bounded layer includes the transmission from the prior interface and the reflection from the next interface. Yet, two exceptions exist. In the first layer, the direct radiation of the acoustic array is present and there is no contribution from transmission from a prior layer. Also, there are no reflected waves in the final layer, which is assumed to be unbounded.

2.3. Ultrasound-induced heat

For the heat resulting from ultrasound, only the thermal contribution in the final layer is taken into account. The consideration of thermal heating in the final layer is taken because most acoustic energy is confined in this region for ablation and because the attenuation coefficient in the final layer, composed from tissue, is appreciably greater than in other layers. In order to map the distribution of heat, the final layer is discretized into volumetric elements, which is an analogy with the surface discretization for the interface in Fig. 2(b). The only difference is that the region of interests turns into volume from surface, and the resulting elements are hexahedral for thermal computation. With the acoustic pressure known from Section 2.2, the temperature rise is computed by the steady-state solution of the bio-heat transfer equation [33].

$$\rho_t C_t \frac{\partial T}{\partial t} = k_t \nabla^2 T - \rho_b C_b W T + Q \tag{8}$$

The T is the temperature change (K) from reference temperature; ρ_t, C_t, and k_t are the density (kg/m^3), specific heat capacity (J/kg/K), and thermal conductivity (W/m/K) of tissue, respectively; ρ_b and C_b are the density and specific heat capacity of blood, respectively; W is the volumetric perfusion rate (m^3/m^3/s) of the blood in the tissue; Q is the thermal power caused by acoustic pressure in unit tissue volume (W/m^3).

For the s^{th} discretized volumetric element, the thermal source caused by the acoustic pressure is

$$Q^s = \alpha_t \frac{\omega}{2\pi} \frac{|p^s_{rms}|^2}{\rho_t c_t} \tag{9}$$

where α_t is the attenuation coefficient (Np/m/Hz) of the tissue, p^s_{rms} is the root mean square value of p^s, and c_t is the sound speed in the tissue.

For the steady state response at one field point [36], the thermal contribution of the s^{th} volume element is

$$T^s = 2\frac{H^s}{|\mathbf{r}_s|} e^{-\frac{|\mathbf{r}_s|}{E}} \tag{10a}$$

$$H^s = \frac{Q^s V_s}{8\pi k_t} \tag{10b}$$

$$E = \left(\frac{k_t}{\rho_b C_b W}\right)^{1/2} \tag{10c}$$

where V_s is the volume of the s^{th} element, $|\mathbf{r}_s|$ is the distance between the center of the s^{th} element and the field point, and the dimensions of H^s and E are (m·K) and (m), respectively.

Since all the discretized volume elements contribute to the thermal response at this field point, hence the overall temperature change is

$$T = \sum_{s=1}^{S} T^s \tag{11}$$

where S is the total number of the discretized volume elements in the tissue.

3. Characterization of deployable tessellated acoustic array

Using the theoretical framework established in Section 2, the ultrasound focusing capability of the proposed concept is characterized in this Section 3. Here, “curved array” is used to refer to the deployable acoustic array based on the curved Miura-ori tessellation. Because the curved array resembles an arc shape, which is an ideal geometry for wave focusing in two dimension [34], a comparison between the curved array and arc is presented for benchmarking purposes. In the comparison, the arc radius, length, and width are the same with those of the corresponding unfolded curved array [27].

3.1. Comparison in focusing between ideal arc and curved array

The focusing and thermal ablation capabilities of the ideal arc and curved array are compared in a 3-layer environment in Fig. 3. The acoustic sources are positioned in water, adjacent to a layer of fat, and then a tissue layer. The layer thicknesses are respectively 2 cm, 2 cm, and 12 cm for the water, fat, and tissue. Material properties for the layers are given in Table 1. The wave focusing is anticipated to occur in the tissue layer based on the curvatures of the arc and array. The curvatures are decided by the folding angle θ that are 4° and 8° for the top and bottom rows in Fig. 3, respectively. The results of acoustic pressure amplitude in Fig. 3(a, b), acoustic intensity in Fig. 3(c, d), and temperature change in Fig. 3(e, f) are shown for the $x-z$ plane where $y = 0$. The facet dimensions of curved Miura-ori unit are $a_1 = 2$ mm, $b_1 = 2$ mm, $\gamma_1 = 75°$, and $\gamma_2 = 70°$, while the size $M_x \times M_y$ is 16×2. Since each Miura-ori unit includes four facets, there is a total of 128 tessellated facets for the tessellation considered in this Section 3. The driving frequency is 1 MHz and the normal velocity amplitude of the oscillating surfaces is 0.3 m/s.

For Fig. 3(a, b), the left portion from $x = 0$ presents the acoustic pressure of the ideal arc while the prediction for the curved array is on the right portion. In the middle unshaded slot of each sub-figure is a black dot that indicates the target focal point. Considering Fig. 3(a) when the curved array is folded to $\theta = 4°$, it is observed that the acoustic pressure amplitude near the target focal region realized from the curved array wave radiation is quantitatively and qualitatively similar to that realized by the ideal arc. The peak locations of acoustic pressure amplitude occur at $z = 10.8$ cm for both the arc and curved array, while the maximum pressure delivered from the curved array to the focal point is approximately 99.0% of the pressure provided by the arc. The deviation on the peak value of the acoustic pressure results from the folding-induced variation of the radiating surfaces of the curved array that reduces the more ideal constructive interference generated by the arc at the focal point [34]. With the increase of folding of the curved array to $\theta = 8°$, Fig. 3(b) shows the curvature radius is decreased and the focal point is closer to the acoustic sources. In this case, there is also substantial qualitative and quantitative agreement in the acoustic fields radiated from the ideal arc and curved array sources both near to the source surfaces and towards the focal point. The peak pressure amplitude from the curved array is 96.5% of the amplitude provided from the arc. The reduction is caused by increase of the folding-induced variation of the curved array source surfaces in the radial direction so that constructive interference at the focal point is mildly reduced.

For both the ideal arc and the curved array, the maximum pressure amplitude in Fig. 3(b) occurs at the designed target focal point of $z = 5.8$ cm. Yet, in Fig. 3(a) the peak pressure amplitude occurs at $z = 10.8$ cm although the focal length inscribed by the source is 11.8 cm. In other words, there is a 1 cm difference between the actual focusing and the targeted location, which is significant for medical treatment. Such deviation is supported by the well-known fact that acoustic focusing occurs closer to the source than the theoretical focal point as the focal length increases [14].

The acoustic intensity around the focal region is shown in Fig. 3(c) and (d). The arrow length indicates the relative intensity magnitude, and the red and blue arrows represent the acoustic intensity of ideal arc and curved array, respectively. For $\theta = 8°$ in Fig. 3(d), it is seen the energy flow substantially converges to the focal point. By comparison, the more parallel intensity vectors in Fig. 3(c) for the longer focal length suggest a less substantial focusing effect. This assessment of results supports the observations to compare Fig. 3(a, b) regarding acoustic pressure amplitude focusing. The red and blue arrows are almost coincident in Fig. 3(c, d), which indicates that the curved array is functionally similar to the ideal arc in terms of the wave focusing mechanisms.

The thermal change from ambient conditions is shown in Fig. 3(e, f). Here, like in Fig. 3(a, b), the thermal changes in the tissue layer induced by the ideal arc are shown to the left portion of the plots while the thermal changes corresponding to wave focusing from the curved array are shown in the right portion. The black dots denote the target focal points. The locations of the maximum temperature rise in Fig. 3(e) and (f) coincide with the peak acoustic pressure in Fig. 3(a) and (b), respectively. On the other hand, the regions of significant temperature rise are spatially broader than the acoustic pressure focusing. This behavior is due to conduction of heat through the tissue layer, a mechanism not found in problems solely of wave propagation. In Fig. 3(e) the temperature is elevated by around 10 K for both the ideal arc and curved array. Yet in Fig. 3(f), the peak temperature rises are 28.39 and 26.51 K for ideal arc and curved array, respectively. This deviation is due to the acoustic pressure amplitude differences provided by the distinct acoustic sources. As Eq. (9) states, the temperature change is determined by the acoustic power. The acoustic power is proportional to the square of acoustic pressure. Using the temperature elevation due

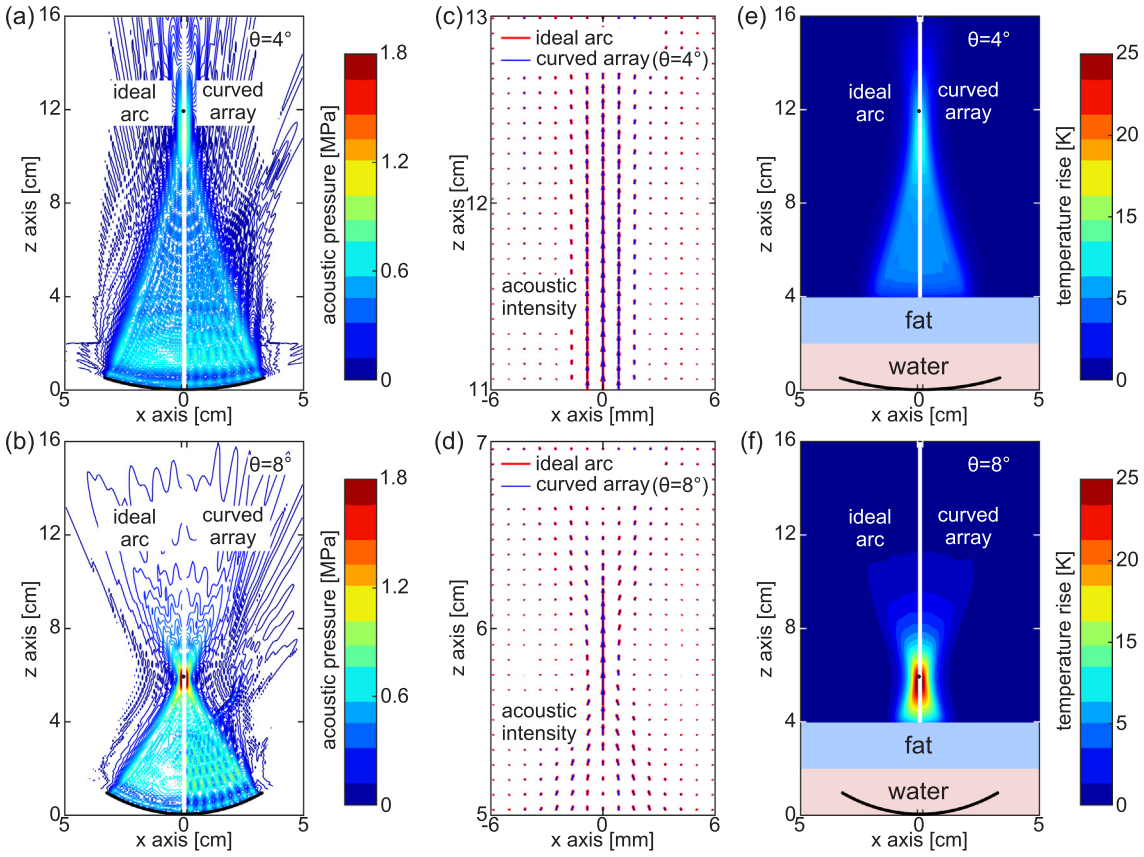

Fig. 3. Comparisons between ideal arc and curved array in the $x - z$ plane of $y = 0$. (a, b) Acoustic pressure amplitude of ideal arc (left) and curved array (right). The black dot in the middle denotes the target focal point and the unshaded area in the bottom indicates the space below acoustic baffle. (c, d) Acoustic intensity of ideal arc (red) and curved array (blue) around focal region. (e, f) Temperature change caused by ideal arc (left) and curved array (right) in the tissue layer. The black dot in the middle denotes the target focal point. Folding angles of tessellated array are 4° (top row) and 8° (bottom row). (For interpretation of the references to colour in this figure legend, the reader is referred to the web version of this article.)

to ideal arc as a reference, the temperature elevation caused by curved array would subsequently approximately be $28.39 \times 0.965^2 = 26.43$ K since the percentage deviation in acoustic pressure amplitude at the focal point (96.5%) should be squared to account for the acoustic power proportionality. This result is close to the actual value of thermal rise caused by the curved array: 26.51 K. This explains the origin of the quantitative temperature difference in Fig. 3(f).

Considering the broad results of Fig. 3 in summary, the peak acoustic pressure amplitude in Fig. 3(a) is around 41% of the amplitude in Fig. 3(b). This quantitatively demonstrates that the significance of acoustic focusing capability is reduced for longer focal lengths. This likewise supports the technical approach that HIFU treatment at close range to the transducer surface results in greater thermal ablation functionality. In the examples given here, the thermal rise increases from 10 K in Fig. 3(e) to around 26 K in Fig. 3(f). Based on the similarity of the thermal change afforded by the curved array compared to the ideal arc, the advantageous deployability of a foldable acoustic array having similar functionality as the ideal arc promotes the detailed consideration of the concept of origami-inspired tessellated arrays to focus ultrasound.

3.2. Contrast in near field region between ideal arc and curved array

Close to the focal regions in Fig. 3, the curved array delivers acoustic waves in functionally similar ways as the ideal arc source. Yet, close to the surfaces of the curved array and arc, Fig. 3 suggests there are greater discrepancies regarding the wave fronts. In order to uncover the underlying physics that distinguishes the tessellated array from the ideal arc source, the acoustic fields near to the transducer surfaces are shown in Fig. 4 for the 1 MHz wave radiation with focal point near $z = 5.8$ cm. Fig. 4(a) presents the acoustic pressure amplitude for the curved array and Fig. 4(b) shows the corresponding results for the arc.

From Fig. 4(a) for the curved array, it is evident that the acoustic field exhibits a periodic sequence of local regions of high acoustic pressure amplitude at constant radial distances to the focal point. Such discrete local foci originate from the near field regions of each unit cell. From the inset in Fig. 4(a), the four facets in each unit point inwardly to a location near to their surfaces. Each unit results in a similar feature,

Table 1
Properties of materials used in multilayer environment [37].

	Speed of sound (m/s)	Density (kg/m^3)	Attenuation coefficient (Np/m/MHz)	Specific heat capacity (J/kg/K)	Thermal conductivity (W/m/K)	Perfusion rate (m^3/m^3/s)
Water	1498	997	2.88×10^{-4}	N/A	N/A	N/A
Fat	1445	921	7	N/A	N/A	N/A
Tissue	1596	1050	4.5	3600	0.512	1.33×10^{-2}
Blood	N/A	1030	N/A	3620	N/A	N/A

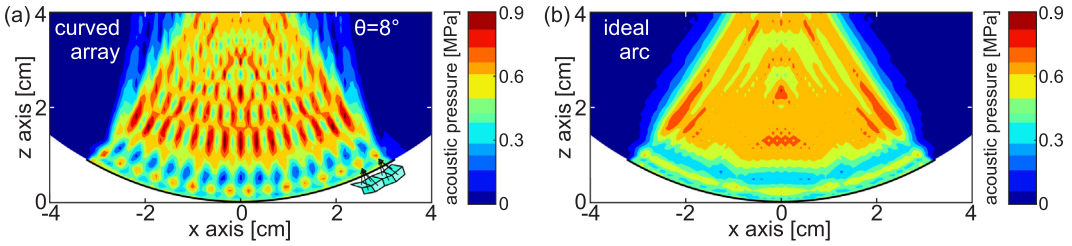

Fig. 4. Near field acoustic pressure of curved array (a) and ideal arc (b) in the $x-z$ plane of $y = 0$, which are the close-ups of Fig. 3(b) in the region close to the acoustic source. In (a), the black circles and white ellipses are for emphasis purpose.

giving rise to the 16 local focal regions adjacent to the array surface. This explains why these spots are uniformly distributed on the curve that is in parallel with the profile of the transducer, and the number of these spots agrees with the number of units in x dimension. Along the propagation of acoustic waves, these local foci eventually converge into the focal point that is designed. In contrast, the acoustic field in Fig. 4(b) is more uniform since the oscillating surface of the arc is smooth and all infinitesimal surface areas are normal to the focal point. These assessments help to illuminate the distinctive constructive interference mechanisms employed by both arrays towards culminating in functionally similar wave focusing.

4. Studies and discussions

In this section comprehensive studies are undertaken to explore strategies to design and deploy the proposed concept of foldable, tessellated arrays for HIFU-relevant practices.

4.1. Acoustic pressure peaks governed by f-number

For a spherical transducer, the f-number relates the focal length with the aperture size [32]. Here an analogy is made for the curved array where the f-number is defined as the ratio of the focal length to the transducer size in the curved dimension, i.e. x direction in this report. To investigate the influence of f-number on focusing, the sizes of the arrays studied in Fig. 5 are (a) 16×2, (b) 12×2, and (c) 8×2. The folding angle for each array remains $\theta = 7^{\circ}$. Consequently, the f-number number is varied from (a) 1.04, to (b) 1.36, to (c) 2.00. Here, the curved Miura-ori unit dimensions, driving conditions, and multi-layer environment parameters are the same with those studied in Section 3. In Fig. 5, the acoustic pressure magnitude at $(x, y) = (0, 0)$ is presented as a function of z axis. Each sub-figure includes the results of transmission ($+z$ direction), reflection ($-z$ direction), and the total response. In the water layer, the direct radiation from the tessellated array is referred to as the transmitted wave. Reflection is not considered in the tissue layer, assuming the layer to extend sufficiently far such that reflected waves are substantially attenuated.

The quality factor is defined to be

$$QF = \frac{z_{peak}}{\Delta z} \tag{12}$$

The z_{peak} is the location in the z-axis where acoustic pressure amplitude is maximized, and Δz is the total distance from z_{peak} over which the acoustic power amplitude is at least one-half of the peak value.

Studying Fig. 5 from (a) to (b) to (c), the focusing capabilities are lessened with the decrease in array units in the long axis. The quality factor is correspondingly reduced according to the array design changes, such that the QF reduces from (a) 6.64, to (b) 3.82, and then to (c) 2.00. The decrease of the quality factor means that the pressure peak becomes broader and therefore the precision of the focused ultrasound is reduced. Moreover, despite possessing the same inscribed radius of curvature, the focal point location in the tissue layer draws closer to the array with reduction of the array units and thus quality factor. Specifically, in Fig. 5(a) and (b), the focal points are near 6.6 cm, which is sufficiently close to the ideal focal length of 6.7 cm. Yet in Fig. 5(c), the focal point is around 5.6 cm. This fact is because acoustic focusing occurs closer to the acoustic transducer of smaller size under the same focal length [14]. From this study, the increase of f-number is not favorable for acoustic focusing, which is analogous to the trend regarding f-number in optics.

In addition, it is seen in Fig. 5 that the contributions from the reflected, backward propagating waves are insignificant to vary the total acoustic pressure amplitude in the near field region. Comparing the total response and the transmission in all sub-figures, the reflection only causes small ripples of the transmission and does not change the total pressure significantly.

4.2. Normal velocity distributions at the layer interfaces

The layer interfaces provide important insight on the focusing capabilities of curved arrays designed with different widths. Here the array width is determined by M_y, i.e. the number of transducer units assembled in y axis. In Fig. 6, the magnitude of the normal particle velocity normalized by M_y is presented over the interfaces. The sizes of the arrays in Fig. 6 are (a) 16×1, (b) 16×2, and (c) 16×3. The folding angle of the arrays is $\theta = 9^{\circ}$. All other variables are the same with those used in Section 3.

Considering the interface at $z = 2$ cm in Fig. 6(a), the velocity

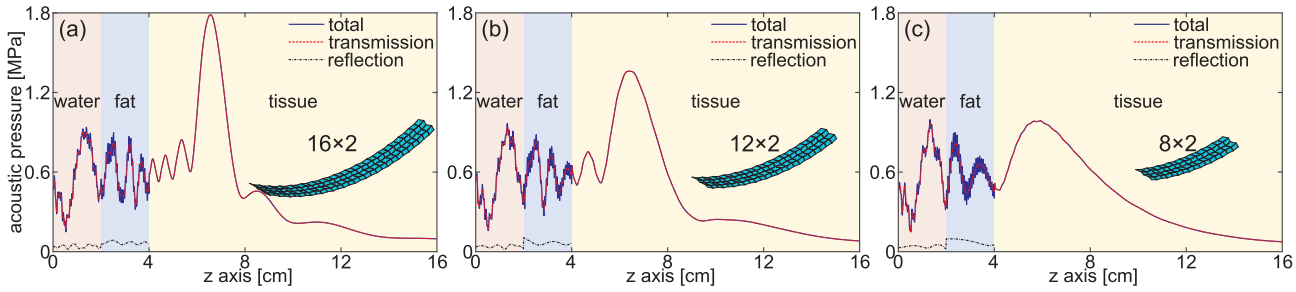

Fig. 5. Magnitude of acoustic pressure at the broadside of tessellated array as a function of axial distance in z direction. Each sub-figure includes the total response, transmission, and reflection. The $M_x \times M_y$ of arrays are 16×2 (a), 12×2 (b), and 8×2 (c). Folding angle is 7° for all the sub-figures.

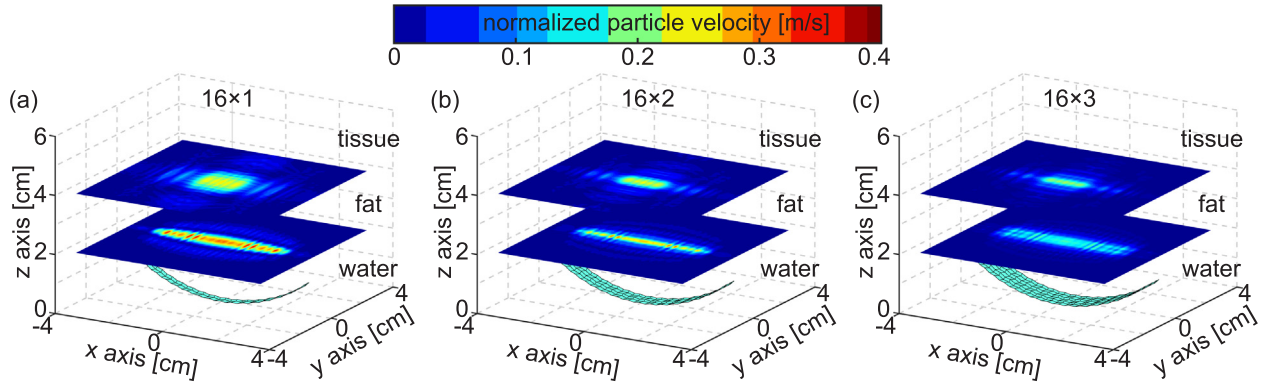

Fig. 6. Magnitude of normal particle velocity over interfaces, which is normalized by number of Miura-ori units in y dimension. $M_x \times M_y$s are 16×1 (a), 16×2 (b), and 16×3 (c). Folding angle is 9° for all the sub-figures.

magnitude exhibits a periodic sequence of locally high values that is distributed along the x direction and narrow in the y direction. The trend originates from similar phenomena as those that produce the periodically large acoustic pressure amplitudes shown in Fig. 4(a). At $z = 4$ cm in Fig. 6(a), such local increases in normal velocity magnitude on the interface are mostly diminished as the waves converge towards the focal point near $z = 5.2$ cm. The area of the large velocity magnitude at $z = 4$ cm is broader in the y dimension than on the interface $z = 2$ cm indicating that focusing from an array shape similar to an arc does not occur in the width dimension.

Similar trends as those observed in phenomena in Fig. 6(a) recur when the number of curved Miura-ori units is increased from 1 to 2 in the y direction in Fig. 6(b). On the other hand, the normalized magnitude of the velocity is decreased overall. Compared with the curved Miura-ori units in Fig. 6(a), the additional assembled units in Fig. 6(b) are further away from the focal point in the y dimension. In practice, the array in Fig. 6(b) is more mechanically robust than the more slender 16×1 array in Fig. 6(a). Due to the greater width for the 16×2 array in Fig. 6(b), a greater proportion of destructive interference occurs in the focal region. The average distances from the oscillating sub-facets of the arrays in Fig. 6(a) and (b) to the arc center are 0.05214 m and 0.05217 m, respectively. The arc radius is 0.05213 m, therefore the phase deviations from ideal focusing caused by the array widths in Fig. 6(a) and (b) are respectively 2.40° and 9.59°. This explains the decrease of the velocity magnitude in Fig. 6(b) compared to results shown in Fig. 6(a). This trend is further extended for the array spanning 16×3 transducer units in Fig. 6(c). Here, the average phase deviation is increased to 24.82°. For the curved tessellated array considered in this study, it is found that the increase in the width dimension diminishes the focusing capability. For acoustics focusing ability in three dimensions, tessellations that emulate spherical shapes are desired [38].

4.3. Influence of tessellation geometry on energy focusing

The geometry of the curved Miura-ori unit also intuitively governs the wave focusing behaviors. In this Section 4.3, the change of edge angle γ_2 is examined for corresponding effects on the acoustic pressure magnitude at focal point. The unit dimensions of curved Miura-ori considered are $a_1 = 2$ mm, $b_1 = 2$ mm, and $\gamma_1 = 55°$. The $M_x \times M_y$ is 16×2 and folding angle θ is 4°. The array elements are driven at 1 MHz with a normal velocity amplitude of 0.3 m/s.

Fig. 7 presents the acoustic pressure amplitude of the curved array as a function of the distance along z axis and edge angle γ_2. The dashed lines denote the geometric radius of the curved array. It is seen that the geometric radius of the curved array, which corresponds to the location of greatest acoustic pressure amplitude, is directly tuned by γ_2. Consequently, this reveals a broad design space by geometry tuning in parallel with array folding to focus waves because the folding angle

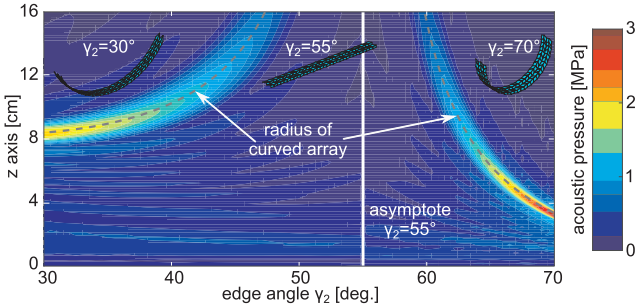

Fig. 7. Broadside acoustic pressure of tessellated array as a function of edge angle γ_2 and z axis. The dashed lines indicate the geometric focal length of curved array and the folding angle is 4°.

remains $\theta = 4°$ in Fig. 7. It is also observed that when the value of γ_2 approaches $\gamma_1 = 55°$, the focal point extends to great distance (beyond the z extent in Fig. 7), and the pressure amplitude is diminished. This fact results from the geometry and can be explained by the limiting case of the middle inset in Fig. 7. From the middle inset, it is seen that $\gamma_2 = 55°$ indicates $\gamma_1 = \gamma_2$ and the curved Miura-ori is equivalent to a regular Miura-ori unit [30]. Because the shape change of a regular Miura-ori array is purely two-dimensional, curvature for focusing is not induced by folding actions. In addition, the geometric radius of the array is more sensitive to changes in γ_2 when $\gamma_2 > \gamma_1$. All together, these results show that the unit geometry complements opportunity to design the tessellated arrays by unit assembly in order to tailor acoustic wave focusing capability.

4.4. Practical considerations of implementation

Drawing on the prior section modeling and studies, the functional characteristics of deployable tessellated array are physically examined and illuminated. Here, practical considerations to implement such a concept are evaluated.

One way to fabricate the transducer elements is through conventional dicing of PZT to shapes that are then bonded to a substrate adopting the crease pattern of the target tessellation, considering practical thick origami principles [39]. To drive the transducer elements and independently actuate the shape, conformal electrical connections [40,41] may then be applied to the PZT network while actuators may be applied to the tessellation hinges or creases. Actuators may include shape memory materials [42,43], magnetic materials [44], or conventional cable-driven techniques. Lamination of the product with fiber-reinforced epoxy, like Garolite or FR4, is one way to enhance the mechanical robustness of the packaged transducer. The actuators may hold the tessellated array into a fully folded shape during transport to the point of care, such as through minimally invasive guided probe

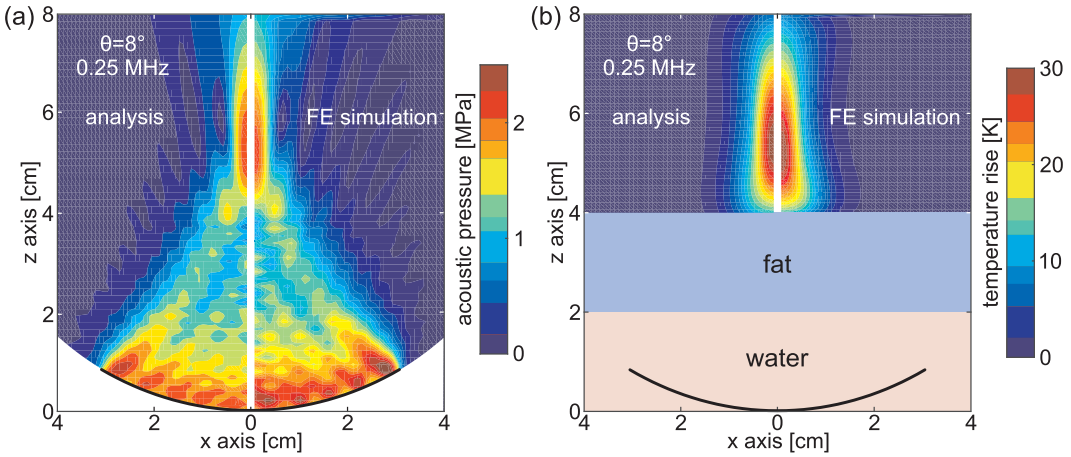

Fig. 8. Comparisons between analysis and FE simulation in the $x-z$ plane of $y=0$. (a) Acoustic pressure predicted by analysis (left) and FE simulation (right). (b) Temperature change predicted by analysis (left) and FE simulation (right) in the tissue layer. Folding angle is 8° and driving frequency is 0.25 MHz.

surgical techniques, and may then be deployed by release of the actuation to reconfigure into the focusing shape. Afterwards the reverse procedures may be undertaken to remove the transducer from the body in the compact and fully folded shape. These are representative ways of implementing the concept in practice although more versatile and effective techniques may be available given continued concept development.

5. Numerical verification

In order to verify the theoretical infrastructure established in Section 2, here the finite element (FE) method is implemented in COMSOL Multiphysics to simulate the wave radiation from the tessellated array into a multilayer domain as a benchmark for analytical predictions. To facilitate the multiphysics computation, the FE model accounts for the heat transfer in the tissue domain, consistent with the analysis. The top and bottom surfaces of the FE simulation boundaries are defined by the temperature distributions computed analytically, since the precise definition of these surfaces is central to the simulation result. The remaining surfaces of the FE simulation utilize ambient temperature definitions. For computational accuracy, the domains are discretized with linear elements using at least six elements along one wavelength. The comparisons of analysis and simulation are presented in Fig. 8. The variables related to the geometry of curved Miura-ori array and multilayered environment are the same with those in Section 3.1. Here, the driving frequency is 250 kHz, due to computational limitations for higher frequency calculations. The folding angle θ is 8° and the normal velocity magnitude of the facets is 1 m/s.

In Fig. 8(a), the left portion of the plot presents the acoustic pressure amplitude predicted by the analysis while the FE simulation results are provided on the right side. The analytical predictions agree well with the simulations considering several distinct qualitative and quantitative aspects of wave focusing. Specifically, the focal regions occur at the same location ($z=5.4$ cm) for both modeling approaches, while the relative error of the peak acoustic pressure magnitude is only 3.8%. Similar conclusions are made for the temperature rise shown in Fig. 8(b). Yet, the discrepancies between analysis and FE simulation are seen away from the focal region in the x axis. The simulations suggest that the thermal energy diffusion adopts an opposite concavity to that of the analysis, seen in Fig. 8(b). On the other hand, the significance of these thermal changes is small in relation to the focal point temperature, since just a 5 mm change in the x direction away from the focal point reduces the thermal rise by almost 15 K. Overall, the agreement in the salient trends of wave focusing between the FE simulation and expedient analysis is good, which underscores the efficacy of the theoretical approach to characterize the versatile wave focusing capabilities of the tessellated arrays.

6. Conclusions

This research investigated an origami-inspired concept of reconfigurable tessellated acoustic arrays for focusing ultrasound and achieving exceptional deployability. By attention to a compact, flat-foldable acoustic array, the analytical studies demonstrate transducer design factors and deployment techniques to achieve thermal elevation levels sufficient for conventional HIFU practice. The interference mechanisms governing the tessellated array wave focusing are contrasted to those of an arc-shaped acoustic source. It is discovered that the tessellated radiator is comparable with the ideal arc in terms of the focal region, while the acoustic responses are distinctive in the field close to transducer surface. Computational simulations verify the efficacy of the theoretical modeling tool and give motivation to the continued development of physically reconfigurable acoustic arrays for ultrasound focusing applications.

Declaration of Competing Interest

The authors declare no conflicts of interest in this submission.

Acknowledgements

This work is supported by the National Science Foundation Faculty Early Career Development Award (No. 1749699).

References

[1] J.E. Kennedy, High-intensity focused ultrasound in the treatment of solid tumours, Nat. Rev. Cancer 5 (2005) 321.
[2] F.A. Jolesz, K.H. Hynynen, MRI-Guided Focused Ultrasound Surgery, CRC Press, New York, 2007.
[3] G. Malietzis, et al., High-intensity focused ultrasound: advances in technology and experimental trials support enhanced utility of focused ultrasound surgery in oncology, Brit. J. Radiol. 86 (2013) 20130044.
[4] T. Kujawska, W. Secomski, M. Byra, M. Postema, A. Nowicki, Annular phased array transducer for preclinical testing of anti-cancer drug efficacy on small animals, Ultrasonics 76 (2017) 92–98.
[5] G.T. Clement, J. White, K. Hynynen, Investigation of a large-area phased array for focused ultrasound surgery through the skull, Phys. Med. Biol. 45 (2000) 1071.
[6] J.E. Kennedy, F. Wu, G.R. Ter Haar, F.V. Gleeson, R.R. Phillips, M.R. Middleton, D. Cranston, High-intensity focused ultrasound for the treatment of liver tumours, Ultrasonics 42 (2004) 931–935.
[7] S. Crouzet, J.Y. Chapelon, O. Rouvière, F. Mege-Lechevallier, M. Colombel, H. Tonoli-Catez, X. Martin, A. Gelet, Whole-gland ablation of localized prostate cancer with high-intensity focused ultrasound: oncologic outcomes and morbidity in 1002 patients, Eur. Urol. 65 (2014) 907–914.
[8] J.F. Aubry, et al., The road to clinical use of high-intensity focused ultrasound for liver cancer: technical and clinical consensus, J. Ther. Ultrasound 1 (2013) 13.

[9] M.R.D. Brown, P. Farquhar-Smith, J.E. Williams, G. Ter Haar, N.M. DeSouza, The use of high-intensity focused ultrasound as a novel treatment for painful conditions—a description and narrative review of the literature, Br. J. Anaesth. 115 (2015) 520–530.
[10] I.R.S. Makin, T.D. Mast, W. Faidi, M.M. Runk, P.G. Barthe, M.H. Slayton, Miniaturized ultrasound arrays for interstitial ablation and imaging, Ultrasound Med. Biol. 31 (2005) 1539–1550.
[11] C. Lafon, J.Y. Chapelon, F. Prat, F. Gorry, J. Margonari, Y. Theillère, D. Cathignol, Design and preliminary results of an ultrasound applicator for interstitial thermal coagulation, Ultrasound Med. Biol. 24 (1998) 1130122.
[12] L.E. Kinsler, A.R. Frey, A.B. Coppens, J.V. Sanders, Fundamentals of Acoustics, John Wiley and Sons, New York, 2000.
[13] K.D. Evans, B. Weiss, M. Knopp, High-intensity focused ultrasound (HIFU) for specific therapeutic treatments: a literature review, J. Diagnostic Med. Sonogr. 23 (2007) 319–327.
[14] G.S. Kino, Acoustic Waves: Devices, Imaging, and Analog Signal Processing, Prentice Hall, New Jersey, 1987.
[15] J.T.B. Overvelde, J.C. Weaver, C. Hoberman, K. Bertoldi, Rational design of reconfigurable prismatic architected materials, Nature 541 (2017) 347–352.
[16] P.M. Reis, F.L. Jiménez, J. Marthelot, Transforming architectures inspired by origami, Proc. Natl. Acad. Sci. 112 (2015) 12234–12235.
[17] K. Fuchi, J. Tang, B. Crowgey, A.R. Diaz, E.J. Rothwell, R.O. Ouedraogo, Origami tunable frequency selective surfaces, IEEE Antennas Wirel. Propag. Lett. 11 (2012) 473–475.
[18] S. Alharbi, S. Chaudhari, A. Inshaar, H. Shah, C. Zou, R.L. Harne, A. Kiourti, E-Textile origami dipole antennas with graded embroidery for adaptive RF performance, IEEE Antennas Wirel. Propag. Lett. (2018), https://doi.org/10.1109/LAWP.2018.2871643.
[19] S. Babaee, J.T. Overvelde, E.R. Chen, V. Tournat, K. Bertoldi, Reconfigurable origami-inspired acoustic waveguides, Sci. Adv. 2 (2016) e1601019.
[20] M. Thota, S. Li, K.W. Wang, Lattice reconfiguration and phononic band-gap adaptation via origami folding, Phys. Rev. B 95 (2017) 064307.
[21] T.G. Leong, C.L. Randall, B.R. Benson, N. Bassik, G.M. Stern, D.H. Gracias, Tetherless thermobiochemically actuated microgrippers, Proc. Natl. Acad. Sci. 106 (2009) 703–708.
[22] N. Bassik, A. Brafman, A.M. Zarafshar, M. Jamal, D. Luvsanjav, F.M. Selaru, D.H. Gracias, Enzymatically triggered actuation of miniaturized tools, J. Am. Chem. Soc. 132 (2010) 16314–16317.
[23] S. Zhu, T. Li, Hydrogenation-assisted graphene origami and its application in programmable molecular mass uptake, storage, and release, ACS Nano 8 (2014) 2864–2872.
[24] Y. Chen, T.T. Zion, W. Wang, R.Y. Kwong, W.G. Stevenson, E.J. Schmidt, Intracardiac MR imaging & MR-tracking catheter for improved MR-guided EP, J. Cardiovasc. Magn. Reson. 17 (2015) P237.
[25] A. Taylor, M. Miller, M. Fok, K. Nilsson, Z.T.H. Tse, Intracardiac magnetic resonance imaging catheter with origami deployable mechanisms, J. Med. Devices 10 (2016) 020957.
[26] M. Johnson, Y. Chen, S. Hovet, S. Xu, B. Wood, H. Ren, J. Tokuda, Z.T.H. Tse, Fabricating biomedical origami: a state-of-the-art review, Int. J. Comput. Assist. Radiol. Surg. 12 (2017) 2023–2032.
[27] C. Zou, R.L. Harne, Adaptive acoustic energy delivery to near and far fields using foldable, tessellated star transducers, Smart Mater. Struct. 26 (2017) 055021.
[28] C. Zou, D.T. Lynd, R.L. Harne, Acoustic wave guiding by reconfigurable tessellated arrays, Phys. Rev. Appl 9 (2018) 014009.
[29] C. Zou, R.L. Harne, Tailoring reflected and diffracted wave fields from tessellated acoustic arrays by origami folding, Wave Motion 89 (2019) 193–206.
[30] J.M. Gattas, W. Wu, Z. You, Miura-base rigid origami: parameterizations of first-level derivative and piecewise geometries, J. Mech. Des. 135 (2013) 111011.
[31] J. Huang, R.G. Holt, R.O. Cleveland, R.A. Roy, Experimental validation of a tractable numerical model for focused ultrasound heating in flow-through tissue phantoms, J. Acoust. Soc. Am. 116 (2004) 2451–2458.
[32] X. Fan, K. Hynynen, The effects of curved tissue layers on the power deposition patterns of therapeutic ultrasound beams, Med. Phys. 21 (1994) 25–34.
[33] H.H. Pennes, Analysis of tissue and arterial blood temperatures in the resting human forearm, J. Appl. Physiol. 1 (1948) 93–122.
[34] C. Zou, R.L. Harne, Piecewise assembled acoustic arrays based on reconfigurable tessellated structures, J. Acoust. Soc. Am. 144 (2018) 2324–2333.
[35] K.B. Ocheltree, L.A. Frizzell, Sound field calculation for rectangular sources, IEEE Trans. Ultrason. Ferroelectr. Freq. Control 36 (1989) 242–248.
[36] W.L. Nyborg, Solutions of the bio-heat transfer equation, Phys. Med. Biol. 33 (1988) 785.
[37] C.W. Connor, K. Hynynen, Bio-acoustic thermal lensing and nonlinear propagation in focused ultrasound surgery using large focal spots: a parametric study, Phys. Med. Biol. 47 (2002) 1911.
[38] H. O'Neil, Theory of focusing radiators, J. Acoust. Soc. Am. 21 (1949) 516–526.
[39] S.A. Zirbel, R.J. Lang, M.W. Thomson, D.A. Sigel, P.E. Walkemeyer, B.P. Trease, S.P. Magleby, L.L. Howell, Accommodating thickness in origami-based deployable arrays, J. Mech. Des. 135 (2013) 111005.
[40] M.D. Dickey, Stretchable and soft electronics using liquid metals, Adv. Mater. 29 (2017) 1606425.
[41] N.C. Sears, J.D. Berrigan, P.R. Buskohl, R.L. Harne, Flexible hybrid electronic material systems with programmable strain sensing architectures, Adv. Eng. Mater. 20 (2018) 1800499.
[42] P. Krulevitch, A.P. Lee, P.B. Ramsey, J.C. Trevino, J. Hamilton, M.A. Northrup, Thin film shape memory alloy microactuators, J. Microelectromech. Syst. 5 (1996) 270–282.
[43] S. Felton, M. Tolley, E. Demaine, D. Rus, R. Wood, A method for building self-folding machines, Science 345 (2014) 644–646.
[44] Y. Kim, H. Yuk, R. Zhao, S.A. Chester, X. Zhao, Printing ferromagnetic domains for untethered fast-transforming soft materials, Nature 558 (2018) 274.